Infrared Physics & Technology 111 (2020) 103537

Contents lists available at ScienceDirect

Infrared Physics and Technology

journal homepage: www.elsevier.com/locate/infrared

Theoretical and experimental study of nanosecond pulse amplification in a CW CO_2 amplifier

Ranran Zhang [a,b], Qikun Pan [a,*], Jin Guo [a], Fei Chen [a], Deyang Yu [a], Junjie Sun [a], Kuo Zhang [a], Luwei Zhang [a]

[a] State Key Laboratory of Laser Interaction with Matter, Changchun Institute of Optics, Fine Mechanics and Physics, Chinese Academy of Sciences, Changchun 130033, China

[b] University of Chinese Academy of Sciences, Beijing 100049, China

ARTICLE INFO

Keywords:
Nanosecond-pulse amplification
Six-temperature model
Dynamic analysis
Pedestal energy

ABSTRACT

With consideration of the temporal characteristics of the electro-optically cavity-dumped seed laser and fast-axial-flow CW amplifier, a mathematical model describing the dynamic process of nanosecond-pulse CO_2 laser amplification is established based on the six-temperature model. This theory perfectly studies the behavior of the CO_2 amplifier gain characteristics and variation in the pulse waveform of a nanosecond input pulse. The dependence of the small-signal gain of the amplifier on the discharge current, gas pressure and ratio of CO_2 and N_2 is studied on theory and experiment, and the evolution of the pulse shape in the gain-extracting stage is simulated. The calculated small-signal gain and output pulse waveforms are in good agreement with the experimental results. The theoretical model can be used to optimize and simulate the amplification performance of a nanosecond-pulse CO_2 laser.

1. Introduction

The nanosecond-pulse CO_2 laser based on Master Oscillator Power-Amplifier (MOPA) plays an important role in the area of extreme ultraviolet (EUV) lithography [1,2]. Using MOPA system, ASML and Gigaphoton Inc have realized tens of kilowatts of CO_2 nanosecond pulse light as the main drive laser [3,4]. CW CO_2 lasers are most frequently used lasers in CO_2-MOPA system for its lower initial and operational costs, robustness, environmental safeness, and reliability. Research on the gain characteristics and dynamic process of nanosecond-pulse CO_2 laser amplification is the focus of this field.

The gain characteristics of the CO_2 laser include a spatial gain distribution and temporal gain evolution. At present, research on the gain characteristics of CO_2 lasers focuses on the spatial models [5–10]. Baeva et al. studied the effects of gas turbulence and convection on the gain of discharge tubes [5,6]. Jelvani et al. studied the effects of the gas velocity and geometric parameters of the discharge tube on the small-signal gain and gas temperature [7]. Nobuaki Takahashi et al. analyzed the spatial distribution of the gain and saturation factors in the discharge tube [8]. The spatial model of a CO_2 laser can be studied with abundant characteristics and parameters. However, the establishment of spatial model is based on spatial differential equations, thus it is not suitable for analysis temporal evolution of gain and other parameters.

Furthermore, the Frantz–Nodvik (F-N) equation is widely used in the study of the gain characteristics of CO_2 amplifiers. F-N equation is suitable for simply evaluating the dependence of output light (pulse width, peak power, waveform, etc.) on the input light parameters and amplifier parameters (small-signal gain, saturation parameter, gain length, etc.) and analyzing the evolution of the pulse waveform during the amplification process [11–13]. However, the F-N equation involves few parameters and cannot fully reveal the dynamic process of nanosecond-pulse-width CO_2 laser amplification.

In 1978, K.Smith and R.M.Thomson first considered the influence of CO and proposed the six-temperature model, which involves abundant energy levels and could obtain the more accurate simulation results and has a wider range of application [14]. It is commonly used to simulate the temporal evolution characteristics of parameters such as the laser gain, vibrational temperature and output pulse shape. It has great potential in studying the dynamic process (temporal characteristics) of short CO_2 laser pulse amplification.

In this paper, based on the six-temperature model, considering the temporal characteristics of a nanosecond-pulse-width CO_2 seed laser and

* Corresponding author.
E-mail address: panqikun2005@163.com (Q. Pan).

https://doi.org/10.1016/j.infrared.2020.103537
Received 12 August 2020; Received in revised form 18 September 2020; Accepted 24 September 2020
Available online 29 September 2020

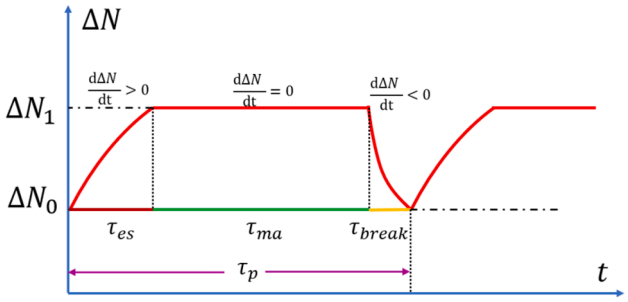

Fig. 1. Schematic diagram of ΔN versus time in a cycle.

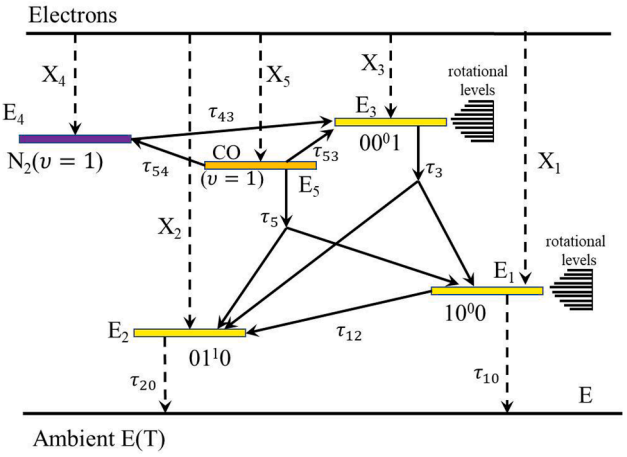

Fig. 2. Schematic energy-level diagram for the N_2–CO_2–CO system.

CW amplifier, the amplification process is divided into three stages, and a dynamic model of nanosecond-pulse amplification is established. The effects of discharge current, gas pressure and gas ratio on the small-signal gain and time variation of the pulse shape are analyzed by this model. An MOPA experiment platform based on a fast-axial-flow amplifier is built. The dependence of the small-signal gain on the discharge current, gas pressure, and gas ratio and the variation in the waveform are studied on experiment, which verifies the theoretical model. The theory of nanosecond-pulse-width CO_2 laser amplification based on the six-temperature model is improved and can be used in the design and optimization of nanosecond-pulse-width CO_2 laser MOPA systems.

2. Theoretical model

2.1. Temporal analysis of the amplification process

The variation of the temperature of each vibrational mode and population inversion between the upper and lower laser levels ΔN of the CW amplifier with a nanosecond-pulse-width seed laser can be divided into three stages (as shown in Fig. 1): the stages of establishing equilibrium, maintaining equilibrium and extracting gain (breaking equilibrium).

In the establishing equilibrium stage, due to the gas discharge, some particles of each vibrational level are excited to the upper level via the processes of electron collision excitation, resonance excitation, energy transfer excitation and charge transfer excitation. The excitation rate of the upper level is faster than the relaxation rate in the amplifier and the photons produced by spontaneous emission cannot effectively consume the population inversion. Therefore, the number density of population inversion continues to accumulate to a saturation value ΔN_1. In the stage of maintaining equilibrium, the temperatures of each vibrational level maintain a dynamic equilibrium due to the counteraction of excitation and relaxation, and the number density of population inversion ΔN remains in the equilibrium state, waiting for the input seed pulse. In the extracting gain stage, after the seed pulse enters the amplifier, the seed light is amplified by the stimulated radiation, the population inversion is consumed rapidly, the gain is reduced, and the temperature equilibrium is broken. When the amplified seed pulse leaves the amplifier, particles in the amplifier return to the establishing equilibrium stage; thus, these three stages are part of a cycle, $\tau_{es} + \tau_{ma} + \tau_{break} = \tau_p$, $\tau_p = 1/f_p$, where f_p is the seed pulse frequency. The parameters τ_{es}, τ_{ma}, and τ_{break} are the durations of the three stages.

2.2. Six-temperature model

Based on the temporal analysis of the amplification process, the evolution of the population inversion number density characterizes the amplification dynamics process of the CO_2 laser amplifier. In this paper, the six-temperature model theory is used to analyze the dynamics of the number density of population inversions in a CW CO_2 amplifier. For short-pulse amplification in CW CO_2 laser, the influence of rotational energy level and vibrational energy level can be determined by τ_{in}/τ_{vv} and τ_{in}/τ_r [15], where τ_{in} is the duration of the input pulse, τ_r and τ_{vv} represent characteristic times for rotational and intramode V-V energy transfer. According to the paper [16], the calculated rotational relaxation time is about 1.5 ns, and the pulse duration is about 10–30 ns, thus the effect of rotational energy transfer is considered [17,18]. In Fig. 2, we present a schematic diagram of the set of processes of electron collision excitation for CO_2, N_2 and CO molecules, all kinds of energy transfer among molecules, and excited emission and spontaneous emission, where E_1, E_2, E_3, E_4, E_5 and E are the stored energy density per unit volume of the CO_2 symmetrical, bending and asymmetrical modes, the N_2 molecule, the CO molecule and its gas mixture. The following Landau–Teller equations describe the time evolution of the energy stored in three different CO_2, N_2, and CO vibrational modes [14]:

$$\frac{dE_1}{dt} = N_e(t) f N_{CO_2} h\nu_1 X_1 + h\nu_1 \Delta N W I_{in}(t) + \left(\frac{h\nu_1}{h\nu_3}\right) \frac{E_3 - E_3(T,T_1,T_2)}{\tau_3(T,T_1,T_2)} - \frac{E_1 - E_1(T)}{\tau_{10}(T)} - \frac{E_1 - E_1(T_2)}{\tau_{12}(T_2)} + \left(\frac{h\nu_1}{h\nu_5}\right) \frac{E_5 - E_5(T,T_1,T_2)}{\tau_5(T,T_1,T_2)} - \frac{E_1}{\tau_F} \tag{1}$$

$$\frac{dE_2}{dt} = N_e(t) f N_{CO_2} h\nu_2 X_2 + \left(\frac{h\nu_2}{h\nu_3}\right) \frac{E_3 - E_3(T,T_1,T_2)}{\tau_3(T,T_1,T_2)} - \frac{E_2 - E_2(T)}{\tau_{20}(T)} + \frac{E_1 - E_1(T_2)}{\tau_{12}(T_2)} + \left(\frac{h\nu_2}{h\nu_5}\right) \frac{E_5 - E_5(T,T_1,T_2)}{\tau_5(T,T_1,T_2)} - \frac{E_2}{\tau_F} \tag{2}$$

$$\frac{dE_3}{dt} = N_e(t) f N_{CO_2} h\nu_3 X_3 - h\nu_3 \Delta N W I_{in}(t) - \frac{E_3 - E_3(T,T_1,T_2)}{\tau_3(T,T_1,T_2)} + \frac{E_4 - E_4(T_3)}{\tau_{43}(T)} + \left(\frac{h\nu_3}{h\nu_5}\right) \frac{E_5 - E_5(T,T_3)}{\tau_{53}(T,T_3)} - \frac{E_3}{\tau_F} \tag{3}$$

$$\frac{dE_4}{dt} = N_e(t) f N_{N_2} h\nu_4 X_4 - \frac{E_4 - E_4(T_3)}{\tau_{43}(T)} + \left(\frac{h\nu_4}{h\nu_5}\right) \frac{E_5 - E_5(T,T_4)}{\tau_{54}(T,T_4)} - \frac{E_4}{\tau_F} \tag{4}$$

$$\frac{dE_5}{dt} = N_e(t)(1-f) N_{CO} h\nu_5 X_5 - \frac{E_5 - E_5(T,T_3)}{\tau_{53}(T,T_3)} - \frac{E_5 - E_5(T,T_4)}{\tau_{54}(T,T_4)} - \frac{E_5 - E_5(T,T_1,T_2)}{\tau_5(T,T_1,T_2)} - \frac{E_5}{\tau_F} \tag{5}$$

$$\frac{dE}{dt} = \frac{E_1 - E_1(T)}{\tau_{10}(T)} + \frac{E_2 - E_2(T)}{\tau_{20}(T)} + \left(1 - \frac{h\nu_1}{h\nu_3} - \frac{h\nu_2}{h\nu_3}\right) \frac{E_3 - E_3(T,T_1,T_2)}{\tau_3(T,T_1,T_2)} + \left(1 - \frac{h\nu_4}{h\nu_5}\right) \frac{E_5 - E_5(T,T_4)}{\tau_{54}(T,T_4)} + \left(1 - \frac{h\nu_3}{h\nu_5}\right) \frac{E_5 - E_5(T,T_3)}{\tau_{53}(T,T_3)} + \left(1 - \frac{h\nu_1}{h\nu_5} - \frac{h\nu_2}{h\nu_5}\right) \frac{E_5 - E_5(T,T_1,T_2)}{\tau_5(T,T_1,T_2)} - \frac{E}{\tau_F} \tag{6}$$

where f is the dissociated fraction of CO_2 molecules. τ_F is the residence time of the gas molecules in discharge, and given by $\tau_F = l/v_g$, where l is the length of the discharge and v_g is the gas flow velocity [19].

$$E = \left(\frac{5}{2}N_{CO_2} + \frac{5}{2}N_2 + \frac{3}{2}N_{He}\right)kT \tag{7}$$

The population inversion between the upper and lower laser levels is

$$\Delta N = N_{001} P(J(001)) - \frac{2J+1}{2J+3} N_{100} P(J+1) \tag{8}$$

where N_{100} and N_{001} is the population number density of the upper and lower levels. The rotational distribution function is given by

$$P(J(001)) = \frac{2hcB_{CO_2}}{kT}(2J+1)exp(-\frac{hcB_{CO_2}J(J+1)}{kT}) \tag{9}$$

B_{CO2} is the rotational constant of the CO_2 molecule, c is the light velocity, h is the Plank constant, k is the Boltzmann constant, T is the gas temperature, and $J(0\,0\,1)$ is the rotational quantum number.

The time evolution of intensity in the amplifier is given by

$$\frac{dI}{dt} = -\frac{I_{in}(t)}{\tau_c} + ch\nu_0 \left[\frac{\Delta N W I_{in}(t)}{h} + N_{oo1} P(J) S\right] \tag{10}$$

where τ_c is the photon life time in the amplifier

$$\tau_c = -\frac{2L}{c(lnR_1 + 2lnR_2)} \tag{11}$$

where R_1 and R_2 are the input and output window mirror reflection (about 1%). The expressions of W and S are

$$W = F\lambda^2/4\pi\upsilon\Delta\upsilon\tau_{sp} \tag{12}$$

$$S = 2\lambda^2 d\upsilon/\pi A\tau_{sp}\Delta\upsilon \tag{13}$$

where λ is the laser wavelength and υ is the laser frequency, $\Delta\upsilon$ is the laser transition line width, $d\upsilon$ is the line width of laser emission, τ_{sp} is the spontaneous emission rate, A is the cross section of the seed laser beam, $F = l/L$ is the filling factor, L is the total optical path in the amplifier.

The laser transition line width is [11]

$$\Delta\nu = \sum_t \frac{N_t Q_t}{\pi}\left[\frac{8kT}{\pi}\left(\frac{1}{M_{CO_2}} + \frac{1}{M_t}\right)\right]^{1/2} \tag{14}$$

here, M_{CO2} and M_t are the masses of molecules, N_t is the number of molecules per unit volume, and Q_t is the collision cross section of the molecules. The stimulated emission is assumed to occur only on the 10P (20) line with 10.59 μm wavelength. The variation of population number inversion density between rotational sublevels of the upper and lower laser vibrational levels is given by the following equation [18]:

$$\frac{d\delta_J}{dt} = -2\delta_J \frac{W}{h} I - \frac{\delta_J - P(J)\Delta N}{\tau_r} \tag{15}$$

The electron density of the pumping process is calculated by the following empirical formula [19]:

$$N_e(t) = \frac{i_0 + i_1 \cos(2\pi f_e t)}{e\pi R_d^2 v_{drift}} \tag{16}$$

where R_d is the discharge tube radius, e is elementary charge and v_{drift} is the drift velocity of the electrons. The i of Eq. (16) is the discharge current and f_e is the linear frequency of the voltage ripple. The discharge current has a time-dependent variation, due to the current ripple introduced by the three rectified phases DC power supply [19].

The dynamic process mainly considers the time variation of the particle number of each vibrational level. The influence of factors such as the turbulence, gas diffusion, and discharge tube geometry on both the gain and the temperature distribution of each vibrational level play a small role in the nanosecond pulse amplification process, which is not discussed in this paper. In order to prevent the light beam from contacting the glass tube, the seed light does not completely cover the (radial) gain area, and the gain uniformity of the seed light coverage area is proved by experiments. It is assumed that the particle number of each vibrational level is evenly distributed in the discharge tube.

2.3. Boundary conditions and numerical methods

The temporal characteristics of the population inversion number density in a seed pulse period can be divided into three stages, it is necessary to set boundary conditions to calculate the initial value to solve the population inversion number density evolution in each stage. This paper mainly analyzes the boundary conditions and numerical calculation methods in the stage of maintaining equilibrium and the stage of extracting gain.

In the stage of maintaining equilibrium, linear frequency of the voltage ripple f_e is about 300 Hz, while seed pulse frequency f_p (10 kHz in this paper) is much faster than f_e, the electron density N_e is considered as a time-independent constant. since the equivalent temperature is constant in the steady state, the steady-state solution can be obtained by making the derivative of the temperature of each vibrational mode equal to zero:

$$\frac{dE_1}{dt} = \frac{dE_2}{dt} = \frac{dE_3}{dt} = \frac{dE_4}{dt} = \frac{dE_5}{dt} = \frac{dE}{dt} = 0 \tag{17}$$

By using the Newton-Raphson method to solve Eq. (17), we can obtain the steady-state temperature value and population inversion number density. The result has the minimum error and quadratic convergence [20]. Since the seed light has not been injected into the amplifier at this stage, $I_{in}(t) = 0$. The small-signal gain g_0 can be calculated by substituting the population inversion number density ΔN into the following formula [21]:

$$g_0 = \Delta N \cdot \frac{A_{21}c^2}{8\pi\upsilon_0^2} g(\upsilon, \upsilon_0) \tag{18}$$

where A_{21} is the coefficient of spontaneous emission, υ_0 is the center frequency of the spectral line, and $g(\upsilon,\upsilon_0)$ is the normalized line shape function.

After the seed pulse leading edge enters the amplifier, with the increase in incident energy, the amplifier enters the extracting-gain stage. In this stage, the temperature of each vibrational level is variable in the

Table 1
Physical parameters used for numerical calculations.

Parameters	Notation (units)	Value
Symmetric excitation rate [22]	X_1 (cm^3/s)	5×10^{-9}
Bending excitation rate [22]	X_2 (cm^3/s)	3×10^{-9}
Asymmetric excitation rate [22]	X_3 (cm^3/s)	8×10^{-9}
N_2 excitation rate [22]	X_4 (cm^3/s)	2.3×10^{-8}
CO excitation rate [22]	X_5 (cm^3/s)	3×10^{-8}
laser wavelength	λ (um)	10.59 (P20)
Rotational constant [22]	B_{CO2} (cm)	0.4
Dissociated fraction of CO_2 molecules [23,24]	f (%)	10
CO_2 symmetric excited level wave number [25]	υ_1/c (cm^{-1})	1337
CO_2 bending excited level wave number [25]	υ_2/c (cm^{-1})	667
CO_2 asymmetric excited level wave number [25]	υ_3/c (cm^{-1})	2349
N_2 excited level wave number [25]	υ_4/c (cm^{-1})	2330
CO excited level wave number [25]	υ_5/c (cm^{-1})	2150
collision cross section of CO_2 molecules [22]	Q_{CO2} (cm^2)	1.3×10^{-14}
collision cross section of N_2 molecules [22]	Q_{N2} (cm^2)	1.14×10^{-14}
collision cross section of He molecules [22]	Q_{He} (cm^2)	3.7×10^{-15}
collision cross section of CO molecules [22]	Q_{CO} (cm^2)	1.14×10^{-14}

process of dynamic change. The number density of photons in the cavity is affected by the number density of incident photons, the gain of the cavity and the stimulated radiation cross section, while the number density of incident photons varies with time. Therefore, the following numerical iterative methods are presented:

We sliced an arbitrary input pulse, $I_{in}(t)$, into M small segments of Δt in the time domain [12]. The total sampling time $\tau_{total} = M \times \Delta t$, where Δt is the sampling interval and M is the sampling time (integer). Each segment is treated as a square pulse. In any segment $t = m$, the recurrence formula for each temperature is as follows:

$$T^{m+1} = \frac{dT^m}{dt}\Delta t + T^m; \qquad (m = 1, 2\cdots M) \tag{19}$$

The recurrence formula for variation of population number inversion density between rotational sublevels:

$$\delta_J{}^{m+1} = \frac{d\delta_J{}^m}{dt}\Delta t + \delta_J{}^m; \qquad (m = 1, 2\cdots M) \tag{20}$$

Output light intensity in segment $t = m$:

$$I_{out}^m = \frac{dI^m}{dt}\Delta t \tag{21}$$

Population inversion:

$$\Delta N^{m+1} = N_{001}|_{T_1^{m+1}, T_2^{m+1}, T_3^{m+1}, T^{m+1}} \cdot P(J(001))|_{T^{m+1}} - \frac{2J+1}{2J+3} \cdot N_{100}|_{T_1^{m+1}, T_2^{m+1}, T_3^{m+1}, T^{m+1}} \cdot P(J+1)|_{T^{m+1}} \tag{22}$$

Time derivative of the light intensity:

$$\frac{dI^m}{dt} = -\frac{I_{in}^m(t)}{\tau_c} + ch\nu_0\left[\frac{\Delta N^m W I_{in}^m(t)}{h} + N^m{}_{oo1}P^m(J)S\right] \tag{23}$$

The amplified output pulse parameters, such as the output power, population inversion and pulse waveform, can be estimated as a function of the seed pulse parameter and amplifier parameter (gas pressure, discharge current, gas ratio, etc.). The physical parameters used for the numerical calculation are summarized in Table 1.

3. Calculated results and experimental analysis

3.1. Experimental device

To verify the model, relevant experiments are designed and carried out. The diagram of the experimental device is shown in Fig. 3. The seed light is produced by an RF-pumped electro-optic cavity-dumped CO_2 laser, and the temporal waveform of which is approximate to Lorentz function. The repetition frequency is continuously tunable from 100 Hz to 30 kHz, the pulse duration is approximately 15 ns, the average power is 1–5 W, the beam waist diameter is 2 mm and the beam divergence angle is about 6 mrad. The amplifier is refitted from a 4000 W fast-axial-

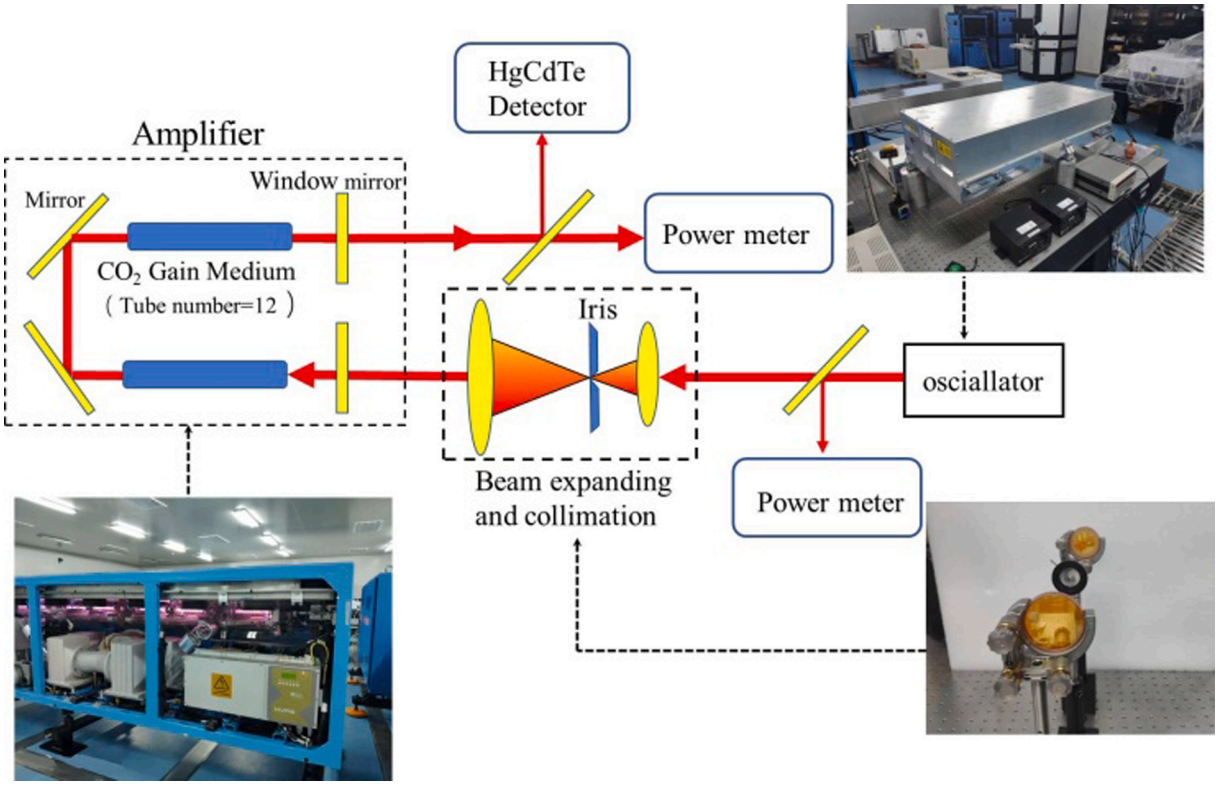

Fig. 3. Diagram of the experimental device.

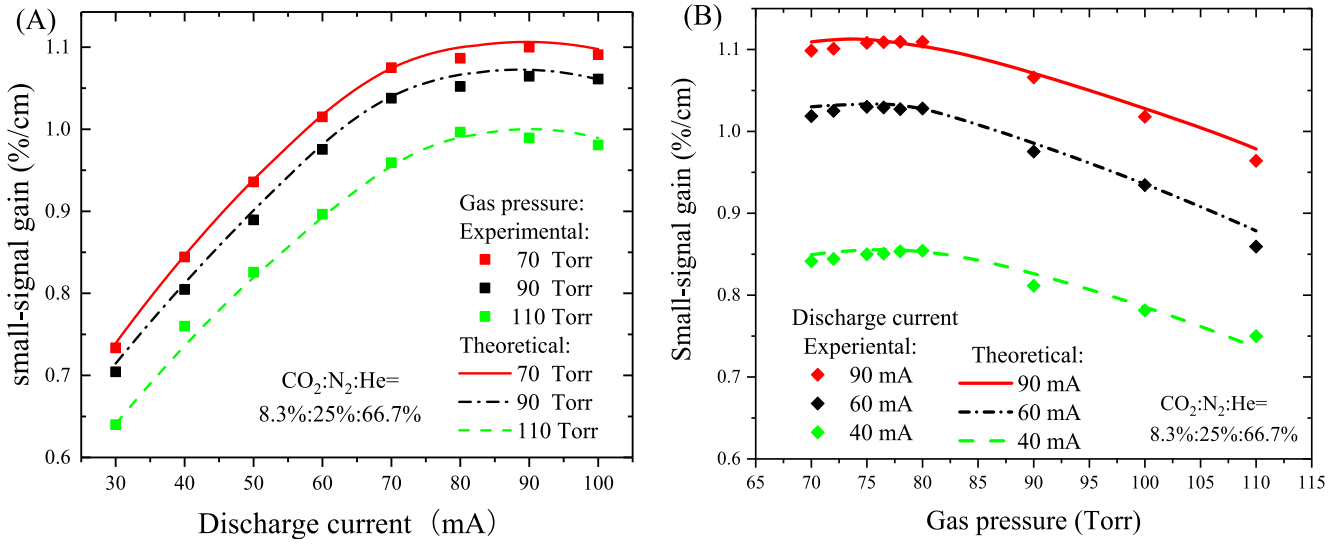

Fig. 4. Small-signal gain versus discharge current (A) and gas pressure (B).

flow laser by replacing two resonator mirrors with ZnSe high-transparent window mirrors. The pumping method of the amplifier is high-voltage DC discharge. The discharge current adjustment ranges from 30 to 100 mA. The gas pressure adjustment range is from 70 Torr to 110 Torr. The ratio of CO_2 to N_2 is adjustable in the range of 1:1.5 to 1:9. The gas velocity is approximately 200 m/s. The total optical path of the amplifier is approximately 450 cm and the total length of discharge tube is 240 cm. The single discharge tube is 20 cm in length and 20 mm in diameter, and the number of discharge tube is 12. The total single-pass loss is approximately 10%. The relationship between amplification and the small-signal gain is as follows

$$B = \exp(g_0 l - \alpha) \tag{24}$$

where α is the single-pass loss factor.

After the seed light leaves the oscillator, it is divided into two beams by the beam splitting mirror. The reflected beam of 1% power enters the power meter to measure the input power in real time, and the transmitted beam of 99% power enters the beam expanding and collimating system. To protect the oscillator and optimize the beam quality, a small aperture is placed at the real focus of the beam expanding and collimating system as a low-pass filter. After beam expansion, filtration and collimation, the beam diameter becomes 15 mm. It enters the discharge tube of the amplifier through the input window, then passes through the gain region and finally leaves the amplifier through a folding mirror and an output window mirror. After the amplified beam leaves the amplifier, it is divided by the second beam splitting mirror. The high-power transmitted light enters the power meter, which measures the output light power, and the low-power reflected light enters the HgCdTe photodetector, which monitors its pulse waveform.

3.2. Simulation and experimental analysis of amplifier gain

Using the established mathematical model, the relationship between the small-signal gain and discharge current, gas pressure, and gas ratio is studied. The relationship between the small-signal gain and discharge current is shown in Fig. 4(A), while the small-signal gain versus gas pressure is shown in Fig. 4(B). As shown in Fig. 4(A), with increasing discharge current, the small-signal gain increases linearly at first and then gradually saturates or even slowly decreases. For the fast-axial-flow amplifier, the discharge current has a linear relationship with the

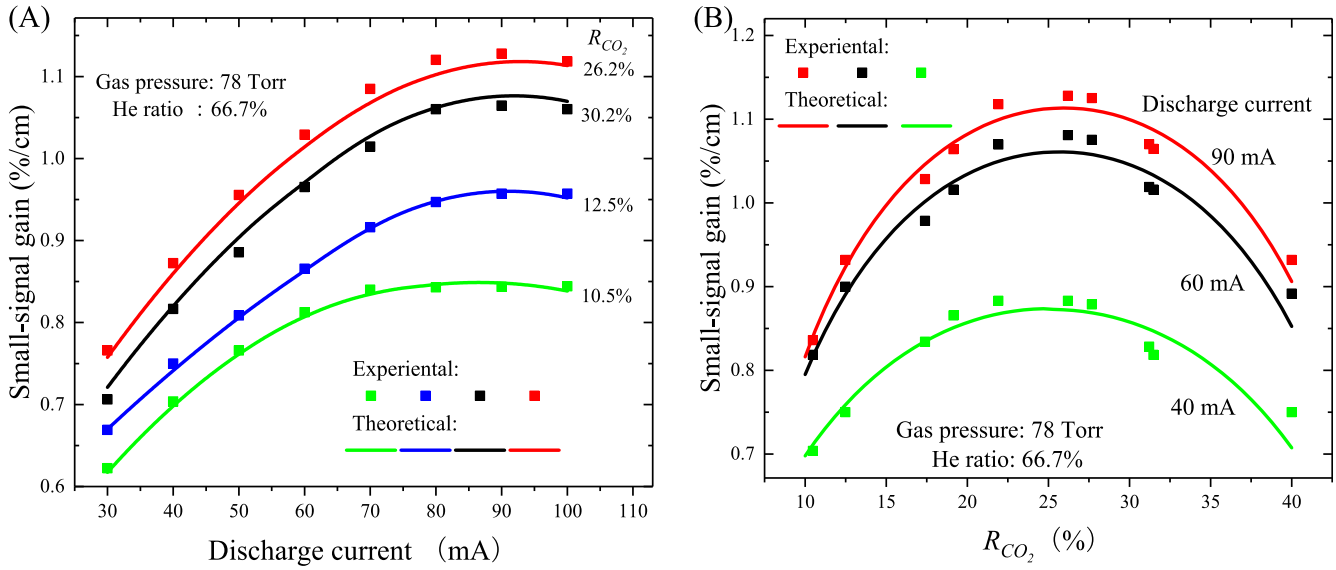

Fig. 5. Small-signal gain versus discharge current (A) and CO_2 relative proportion (B).

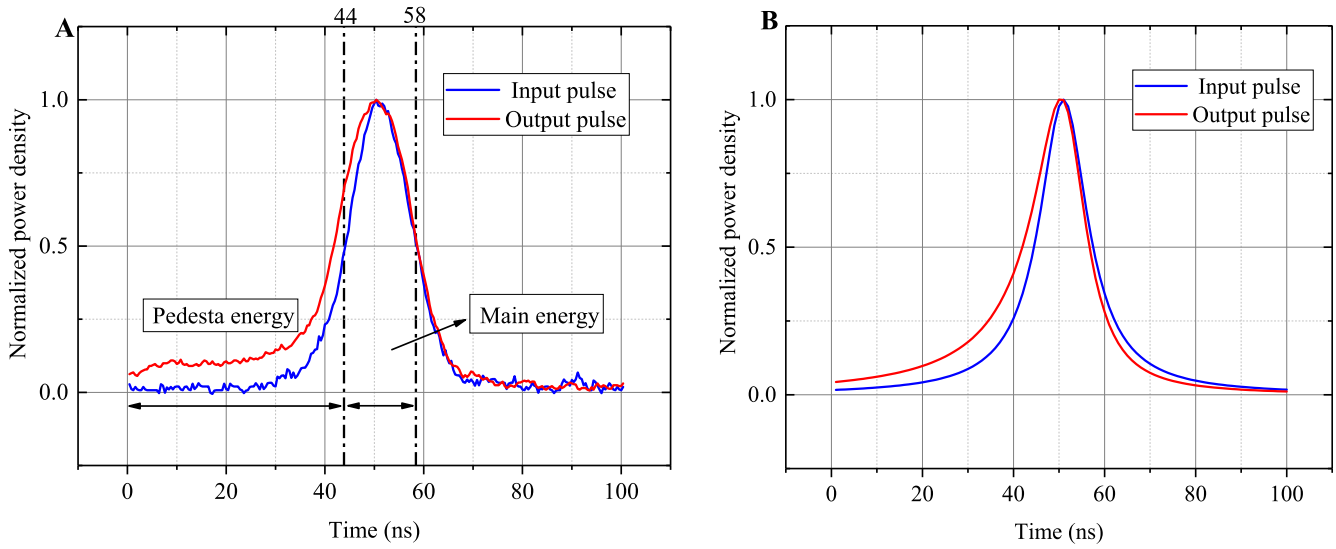

Fig. 6. The measured (A) and theoretical (B) shape of the input and output pulse.

electron density. With increasing discharge current, the number of electrons increases which leads to the heating of the laser gas is due to collisions of electrons with molecules. The gas temperature and discharge current shows an almost linear relationship, however, it becomes exponentially at higher currents [8]. The rapidly increase in the gas temperature is not conducive to the accumulation of upper-level particles, and the relaxation rate of antisymmetric vibrational levels accelerates, resulting in a decrease in the small-signal gain after saturation. Therefore, a proper increase in the discharge current can result in an increase in the small-signal gain, but the small-signal gain will decrease if the discharge current is over saturated.

In addition, the gas pressure of the amplifier has a significant effect on the small-signal gain. For the fast-axial-flow CO_2 laser, on the one hand, the saturation population inversion number density increases with raise of the gas pressure, which is beneficial to achieving an increase in the small-signal gain. On the other hand, the raise of the gas pressure results in promoting for the relaxation rate of antisymmetric vibrational mode particles. The two factors determine the small-signal gain. As the experimental results show, the small-signal gain at a gas pressure of 75–80 Torr is higher than that at any other gas pressure, and the small-signal gain increases more at 75–80 Torr when the current is increased by 10 mA each time. The peak small-signal gain appears between gas pressures of 75 and 80 Torr for our experimental device, and the simulation results are consistent with the experimental results.

The variations in the small-signal gain with the relative proportion of CO_2 and the discharge current are shown in Fig. 5. Define the relative proportion of CO_2 as

$$R_{CO_2} = \frac{x}{x+y}(\%) \tag{25}$$

where x (%) is the CO_2 ratio and y (%) is the N_2 ratio. With increasing discharge current, the small-signal gain also exhibits the phenomenon of gain saturation, and the relative proportion of CO_2 has a significant effect on the small-signal gain. With the gas pressure fixed at 78 Torr and He ratio fixed at 66.7%, the small-signal gain versus discharge current is calculated at different relative proportion of CO_2 from 10% to 40%. Fig. 5(A) shows four curves of $R_{CO2} = 10.5\%$, 12.5%, 26.2% and 30.2%. As shown in Fig. 5(A), for $R_{CO2} = 10.5\%$, when the discharge current is greater than 70 mA, with increasing discharge current, the small-signal gain increases, but the trend slows down, which indicates that electron densities are not fully utilized and that the gas pressure and ratio need to be further optimized. After adjusting the CO_2 relative proportion several times, such as $R_{CO2} = 26.2\%$, the small-signal gain obviously increases with increasing discharge current, and R_{CO2} is close to the optimal value. In fact, the N_2 ratio has two effects on the population inversion number density. First, when the gas pressure and He ratio are fixed, increasing the N_2 ratio leads to a decrease in the CO_2 molecular density N_{CO2}, which results in the decrease of the saturation population inversion number density. Second, the main role of N_2 in the CO_2 laser amplifier is to accelerate the accumulation of the population inversion number density through the resonance energy transfer between its excited state ($V = 1$) and antisymmetric vibrational level (the excitation rate X_4 of the N_2 molecular vibrational mode is approximately 2–3 times that of the CO_2 molecular vibrational mode). The two effects determine the optimal ratio of CO_2 to N_2. The small-signal gain variation with the CO_2 relative proportion at different discharge currents is shown in Fig. 5(B). Their relationship is similar to the sine function, and the peak value of the small-signal gain is obtained at approximately $R_{CO2} = 25\%$. Again, the theoretical data fit the experiments well.

The experimental and simulation results show that the discharge current, gas pressure, and ratio of CO_2 to N_2 have a significant effect on the small-signal gain. By optimizing the gas pressure and ratio of the amplifier, when the discharge current is 100 mA, the gas pressure is 78 Torr, and the ratio of CO_2:N_2:He = 1:3:6, the peak small-signal gain is obtained. The optimized amplification is about 12 times (2.8 to 33.6 W/

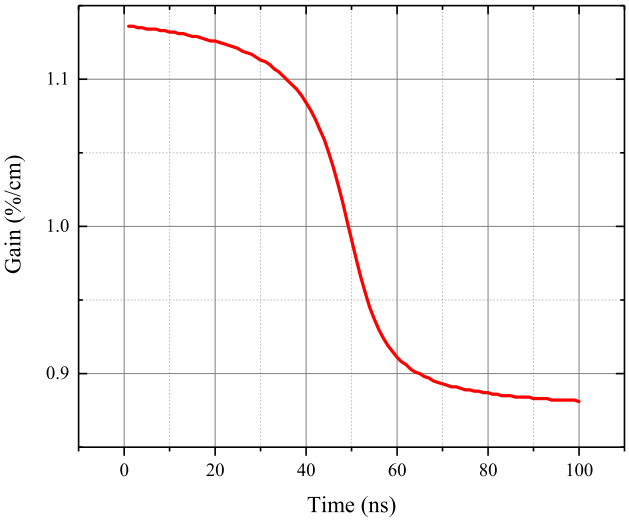

Fig. 7. Gain versus time in the extracting-gain stage.

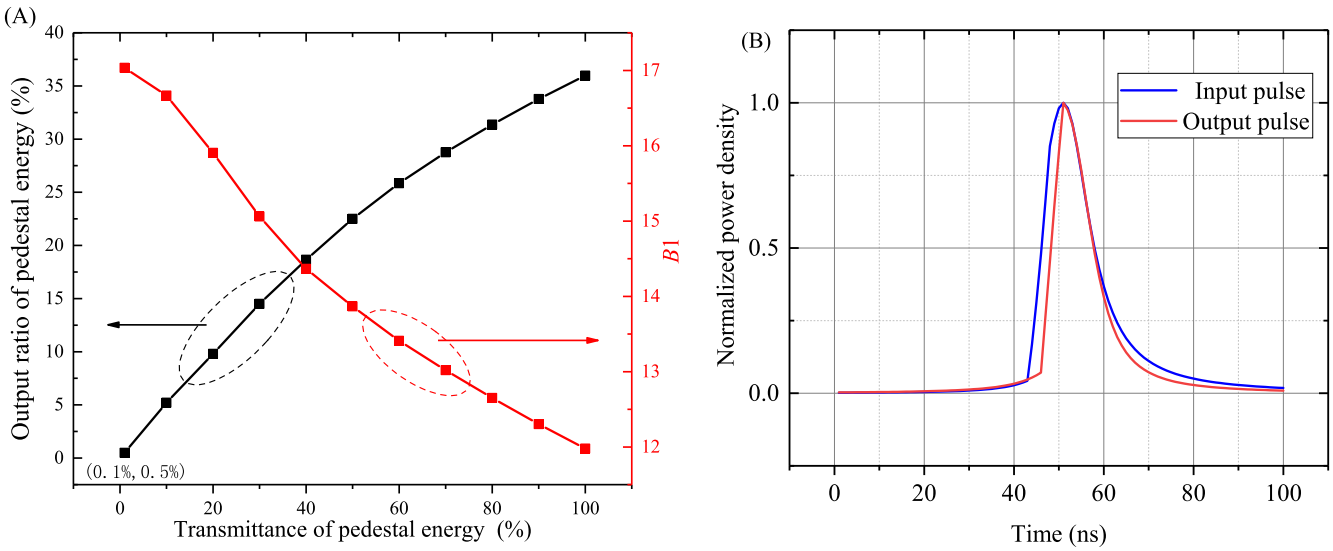

Fig. 8. (A) Theoretical output ratio of pedestal energy and $B1$ verse transmittance of pedestal energy. (B) Theoretical shape of the input and output pulse when transmittance of pedestal energy is 10%

cm^2), which is significantly improved compared with the initial amplification of 5 times.

3.3. Simulation and experimental analysis of temporal pulse shape evolution

The temporal shape of the CO_2 pulse affects the conversion efficiency of the CO_2 laser to extreme ultraviolet light in the LPP-EUV system [26]; thus, research on the evolution of the pulse shape in the amplification process is helpful for the design and optimization of the MOPA system. For the extracting-gain stage, the calculation method in Section 2 is used to simulate the temporal variation of the population inversion number density, small-signal gain and output pulse shape in the amplification process. The simulated and experimental results with input and output pulse shapes are compared in Fig. 6. The amplifier gas pressure is 78 Torr, the ratio is CO_2:N_2:He = 8.3%:25%:66.7%, the discharge current is 100 mA, the input pulse width is 14 ns, the repetition frequency is 10 kHz, and the average input power is 5 W. The duration of the simulation input pulse is about 14 ns (FWHW), the sampling interval $\Delta t = 1$ ns, and the sampling times $M = 100$. The input and output pulse shapes overlap at the peaks in the shape comparisons. The simulation pulse shape fit the experiments well. The experimental average output power is about 60 W, the simulated average output power is 58.6 W. The experimental output pulse width is approximately 16 ns, the simulated output pulse width is 15 ns, and the power density in 0–44 ns of the output pulse in the two figures has an obvious upward trend compared with the pulse trailing edge.

As far as we know, there is no clear quantitative standard for the pedestal energy, so we defined the energy within 0–44 ns of the pulse as the pedestal energy and the energy within 44–58 ns (FWHW for input pulse) as the main energy. The pedestal energy of the input pulse accounts for 25.6% of the total pulse energy, while the pedestal energy of the output pulse accounts for 36%. The raise in the ratio of pedestal energy is due to the priority consumption of the prior incident photons of input pulse on the amplifier gain, namely, the population inversion. The simulated variation in the gain in the amplification process is shown in Fig. 7. In the gain-extracting stage, with increasing incident pulse energy, population inversion decreases due to the stimulated radiation. However, the input pulse width is only approximately 14 ns, and consumed population inversion cannot be supplemented by the direct excitation of electrons to CO_2 molecules or the resonant energy transfer process between N_2 (and CO) and CO_2 molecules. Hence, the gain decreases rapidly and saturates gradually, which results in the raise of ratio of pedestal energy.

Pedestal energy is a kind of temporal pulse distortion, which widely exists in many amplifiers and reduces the main energy amplification and may damage the stability of the MOPA system. In EUV-LPP system, another hazard of pedestal energy is that it reduces the conversion efficiency of CO_2 light to 13.5 nm light [26], so it needs to be isolated. Measures such as electro-optic isolation (CdTe Pockels Cell and polarizer) or saturated absorption isolation (such as SF_6) can decrease the input ratio of pedestal energy. Define the main energy amplication as $B1$. As shown in Fig. 8(A), with the transmittance of pedestal decreased from 100% to 1%, the output ratio of pedestal energy to total pulse decreases from 36% to 0.5%, the $B1$ increases from about 12 to 17 times. As shown in Fig. 8(B), with set tranmittance of input pedestal energy as 10%, the output pedestal energy is effectively suppressed and the pulse leading edge becomes steep.

It can be concluded that the ratio of pedestal energy will increase in the nanosecond CO_2 amplification process, and isolation measures can effectively suppress the output pedestal energy, which is conducive to pulse shape optimization and increase of the main energy amplification.

4. Conclusions

In this paper, considering the temporal characteristics of a nanosecond-pulse CO_2 seed laser and CW amplifier, a mathematical model is established based on the six-temperature model, and the amplification process is divided into three stages according to periodic evolution of the population inversion number density. Parameters such as the output power, population inversion and pulse waveform, etc., can be estimated as a function of the seed pulse parameter and amplifier parameter (gas pressure, discharge current, gas ratio, etc.). Both the experimental and theoretical results present the following: First, the gas pressure, gas ratio and discharge current greatly affect the small-signal gain. When the discharge current is about 100 mA, the optimal gas pressure is about 78 torr and ratio of CO_2 to N_2 is about 1:3 in our experiment. Second, the input pedestal energy is amplified prior to the main energy, which causes the raise in the output ratio of pedestal energy and need to be isolated. The theoretical model can be used to optimize and simulate the amplification performance of a short-pulse CO_2 laser.

Declaration of Competing Interest

There are no conflicts of interest to declare.

Acknowledgements

The authors want to acknowledge the support provided by 'National Natural Science Foundation of China' (Grant No. 61675200, Grant No. 61904178 and Grant No. 61705219), 'Jilin Province Science and Technology Development Plan Project' (Grant No. 20190103133JH), 'State Key Laboratory of Laser Interaction with Matter Project' (Grant No. SKLLIM1814 and Grant No. SKLLIM1914), 'The open fund project of the state key laboratory of Laser and material interaction' (Grant No. SKLLIM1712).

References

[1] J. Fujimoto, T. Hori, T. Yanagida, H. Mizoguchi, Development of laser-produced tin plasma-based euv light source technology for HVM EUV lithography, Proc. SPIE 8322 (2012) 12.
[2] H. Mizoguchi, H. Nakarai, T. Abe, K. M. Nowak, and T. Saitou, "Development of 250W EUV light source for HVM lithography," in China Semiconductor Technology International Conference (2016).
[3] T. Yabu, T. Yanagida, Y. Kawasuji, T. Hori, K. Miyao, Key components development progress updates of the 250W high power LPP-EUV light source, Int. Conf. Extreme Ultraviolet Lithography (2017).
[4] D.C. Brandt, I.V. Fomenkov, N.R. Farrar, B.L. Fontaine, S.D. Rich, CO2/Sn LPP EUV sources for device development and HVM, Spie Advanced Lithography (2013).
[5] M.G. Baeva, P.A. Atanasov, Numerical investigation of CW CO $_2$ laser with a fast turbulent flow, J. Phys. D Appl. Phys. 26 (4) (1993) 546–551.
[6] S. Muller, J. Uhlenbusch, Influence of turbulence and convection on the output of a high-power CO_2 laser with a fast axial flow, Br. J. Appl. Phys. 20 (1987) 697–708.
[7] S. Jelvani, H. Saeedi, Numerical investigation of a fast-axial-flow CW CO_2 laser, Opt. Laser Technol. 40 (3) (2008) 459–465.
[8] N. Takahashi, E. Tsuchida, H. Sato, Spatial variation of gain and saturation in a fast axial flow CO_2 laser amplifier, Appl. Opt. 28 (1989) 3725–3736.
[9] Huang, Hongyan, and Y. Wang . "Kinetic modeling and optimum design of the discharge tube for the CO2 laser with computational fluid dynamics method." Opt. Eng. 49,114201.1-114201.7 (2010).
[10] A.M. Koushki, K. Silakhori, S. Jelvani, Kinetic modeling of a slow flow CW CO_2 laser, Opt. Quant. Electron. 43 (1-5) (2012) 23–33.
[11] L.M. Frantz, J.S. Nodvik, Theory of pulse propagation in a laser amplifier, J. Appl. Phys. 34 (1963) 2340–2346.
[12] J. Jeong, S. Cho, T.J. Yu, Numerical extension of Frantz–Nodvik equation for double-pass amplifiers with pulse overlap, Opt. Express 25 (4) (2017) 3946, https://doi.org/10.1364/OE.25.003946.
[13] P. Daewoong, J. Jihoon, J. Tae, Yu, Optimization of the pulse width and injection time in a double-pass laser amplifier, High Power Laser Sci. Eng. (2018).
[14] K. Smith, R.M. Thomson, Computer modeling of gas lasers, New York: Plenum Press 25–78 (1978).
[15] R.J. Harrach, Effect of rotational and intramode vibrational coupling on short-pulse amplification in CO_2, IEEE J. Quantum Electron. 11 (1975) 349–357.
[16] Ralph R. Jacobs, Kenneth J. Pettipiece, Scott J. Thomas, Rotational relaxation rate constants for CO_2, Appl. Phys. Lett. 24 (8) (1974) 375–377.
[17] R. Torabi, H. Saghafifar, A.M. Koushki, Theoretical and experimental analyses of the TEA CO2 lasers dynamics by six temperature vibrational-rotational model, Optik 135 (2017) 238–243.
[18] Y. Qu, D. Ren, L. Zhang, X. Hu, and F. Liu, "Five temperature mathematical modeling of TEA CO2 laser," in Atomic and Molecular Pulsed Lasers VI, (2006).
[19] Sharif Al-Hawat, Kheir Al-Mutaib, Numerical modeling of a fast-axial-flow CW–CO_2 laser, Opt. Laser Technol. 39 (3) (2007) 610–615.
[20] M. Chrzanowskajeske, R.C. Jaeger, Steady-state bipolar transistor simulator for the 77 K-300 K temperature range, IEEE Custom Integrated Circuits Conference IEEE (2012).
[21] Wild Sazhin, et al., The three temperature model for the fast-axial-flow CO_2 laser, Br. J. Appl. Phys. 26 (1993) 1872–1883.
[22] M. Soukieh, B.A. Ghani, M. Hammadi, Mathematical modeling of CO2 TEA laser, Opt. Laser Technol. 30 (1998) 451–457.
[23] Nighan, L. William, Effect of molecular dissociation and vibrational excitation on electron energy transfer in CO 2 laser plasmas, Appl. Phys. Lett. 15 (11) (1969) 355–357.
[24] E. Lotkova, V. Ochkin, N. Sobolev, Dissociation of carbon dioxide and inversion in CO2 laser, IEEE J. Quantum Electronics QE 7 (1971) 396–402.
[25] K. Rossmann, W.L. France, K.N. Rao, H.H. Nielsen, Infrared spectrum and molecular constants of carbon dioxide, J. Chem. Phys. 24 (1956) 1007–1008.
[26] A.A. Schafgans, D.J. Brown, I.V. Fomenkov, R. Sandstrom, R. Kool, Performance optimization of MOPA pre-pulse LPP light source, SPIE Advanced Lithography (2015).